Concurrent Photothermal Therapy and Nuclear Magnetic Resonance Imaging with Plasmonic-Magnetic Nanoparticles: A Numerical Study

C. Rousseau,[1] Q.L. Vuong,[2] Y. Gossuin,[2] B. Maes,[1] and G. Rosolen[1]

[1] *Micro- and Nanophotonic Materials Group, Research Institute for Materials Science and Engineering, University of Mons, 20 Place du Parc, B-7000 Mons, Belgium*

[2] *Biomedical Physics Unit, University of Mons, 20 Place du Parc, B-7000 Mons, Belgium*

Background and Objective: Theranostics is the combination of the diagnostic and therapeutic phases. Here we focus on simultaneous use of photothermal therapy and magnetic resonance imaging, employing a contrast-photothermal agent that converts incident light into heat and affects the transverse relaxation time, a key magnetic resonance imaging parameter. Our work considers a gold-magnetite nanoshell platform to gauge the feasibility of magnetic resonance imaging monitoring of the heating associated with phototherapy, by studying the modification of the transverse relaxation rate induced by laser illumination of a solution containing these hybrid nanoparticles.

Methods: We simulate a system composed of an aqueous solution with hybrid nanoshells under continuous laser irradiation, enabling the evaluation of spatial variations of the transverse relaxation rate within the sample. We work with the hybrid nanoshell platform comprising a metal/gold shell for thermoplasmonic effects and a magnetite core for magnetic resonance imaging contrast enhancement. The optical properties of the nanoshells are first obtained through simulations using the finite element method. Next, the heating generated by the laser illumination is calculated by numerical integration. Finally, the transverse relaxation rate is obtained through the application of an analytical model. Additionally, we conduct an optimization of the nanoshell geometry to fulfill requirements of both magnetic resonance imaging and phototherapy techniques.

Results: Our findings demonstrate a narrow range of nanoshell sizes exhibiting both a plasmonic absorption peak in the human biological window and a high response to laser illumination of the transverse relaxation rate. Furthermore, the illumination can induce up to a 30% modification in transverse relaxation rate compared to the non-illuminated scenario in this range of nanoshell sizes.

Conclusions: In this work we establish the numerical understanding of the interplay between phototherapy and nuclear magnetic resonance imaging when employed concurrently. This allows magnetic resonance imaging monitoring of the heating associated with phototherapy.

Keywords: Theranostic agents, Phototherapy, Magnetic Resonance Imaging, Thermoplasmonics

I. INTRODUCTION

In recent years extensive research was conducted on theranostics, a medical field combining the diagnostic and therapeutic phases[1]. Furthermore, a variety of inorganic nanomaterials has been developed for different medical applications. For example, these nanomaterials include nano-morsel of semiconductors (for quantum dots), carbon nanotubes, porous silica nanoparticles (NPs)[2]. These different platforms enable various combinations of imaging methods and treatment approaches. Among these technical combinations, the integration of nuclear magnetic resonance imaging (MRI) and photothermal therapy is important in the literature[3–6]. This can be explained by the fact that during an MRI examination, a

contrast agent is often used to enhance the obtained image by modifying the relaxation of the protons in the tissues[7]. Therefore, theranostics can be achieved by modifying this agent to add the capability of providing additional photothermal therapy.

Photothermal therapy relies on a photothermal agent capable of converting incident light energy into heat to kill cancer cells[8]. The temperature increase required to damage cancer cells ranges between 3 and 7 °C[9]. When a gold NP is illuminated with laser light, localized surface plasmons can be excited in the metal shell, which refers to a normal mode of collective oscillation of the free electrons contained in the metal[10]. For strong excitation to occur, the frequency of the incident light must match the plasmonic resonance frequency of the NP. This frequency is influenced by several factors, including the NP composition, geometry, and the characteristics of the surrounding medium. This free electron oscillation, driven by the Joule effect, converts incident light energy into thermal energy. Subsequently, this thermal energy is dissipated into the surrounding medium, resulting in a temperature rise[10]. For biomedical applications the plasmonic metal is predominantly gold due to its biocompatibility[11].

MRI contrast agents can be divided into two main types[12]: Paramagnetic complexes, which include gadolinium ions, and superparamagnetic particles, mainly composed of magnetite or maghemite NPs. The latter category can be modified to transform the particle into a combination of a contrast and a photothermal agent, by adding a metallic plasmonic shell, thus forming a magnetic-plasmonic nanoshell (NS) platform[13]. An exemple of an NS configuration, studied in this work, is shown in Fig. 1a, with the magnetite core radius (r_{core}) and shell thickness (t_{shell}) indicated.
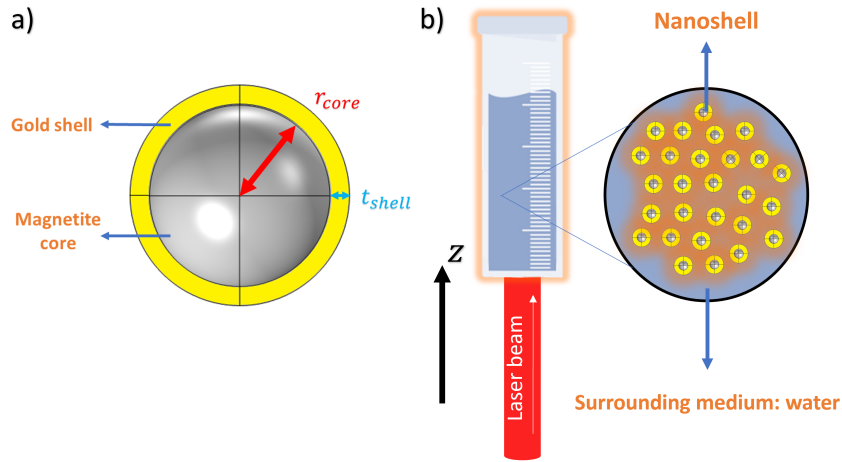

FIG. 1.   Combination of MRI and photothermal therapy with NS platform. (a) NS with a magnetite core as MRI agent and a gold shell as photothermal agent. (b) The considered setup: An aqueous solution of NSs under laser illumination.

There are various methods for adding the gold shell around the magnetite core, such as co-precipitation, thermal decomposition, and reversed micelle techniques[14]. Some synthesis methods allow to obtain magnetite-gold NSs with good water solubility, which can be further increased by adding a coating around the NS[15]. The NS configuration offers many advantages, such as the high tunability of its plasmonic resonance[16], easy functionalizability for achieving effective targeting of cancer cells[17], and biocompatibility[18].

This study aims at numerically estimating the relaxation induced by a contrast-photothermal agent during a phototherapy treatment. The goal is to investigate the possibility of finding a NS geometry that would enable real-time monitoring of temperature elevation due to MRI-guided phototherapy. To this end, we combine two fields of study: Thermoplasmonics (by plasmonic particles) and MRI relaxation (by superparamagnetic particles) to model the behavior of an ideal aqueous solution. Our numerical method computes the spatial

distribution of the modification of the transverse relaxation rate R_2 in a NS solution,due to the temperature increase produced by the (continuous-wave) laser illumination. This modeling of temperature elevation takes into account collective thermal effects among the NSs. The iron concentration is adjusted to 0.2 mM, a realistic concentration in a tumor after intravenous injection of a solution of NPs[19]. Depending on the MRI relaxation regime, appropriate effective methods to calculate R_2 are identified and employed.

The numerical study of the optical properties of gold-magnetite nanoshells has already been carried out in the literature[20]. The temperature increase generated by laser illumination of such structures has also been addressed in the literature both experimentally and numerically[21,22]. However, the optimization of the NS geometry with the aim of utilizing this platform as a theranostic agent has never been achieved. These results fill a gap in the joint study of MRI and photothermal therapy, and enables us to assess the possible outcomes of using both photothermal therapy and MRI as part of a theranostic examination. Our results show that, for specific NS geometries, the illumination can induce up to a 30% modification in R_2 compared to the non-illuminated scenario, in addition to generating a sufficient temperature increase for phototherapy. MRI could thus be used to monitor the temperature increase caused by the photothermal therapy for NSs with a r_{core} in the range of 20-25 nm range and t_{shell} of 10 nm.

This article is structured as follows: Section II is dedicated to detailing the calculation methods used in this work. This initial section is divided into three subsections, each addressing a distinct aspect of the method: Optical simulations (Subsection II A), collective thermal effects (Subsection II B), and relaxation induced by superparamagnetic NPs (Subsection II C). Section III focuses on the obtained results. This latter section is also subdivided into three parts: The first one deals with optical results (Subsection III A), the second describes the results obtained for temperature elevation following laser illumination (Subsection III B), and the last part addresses the modification of relaxation induced by this temperature increase (Subsection III C).

II. CALCULATION METHODS

In this section we detail the three modeling steps, within the context of a phototherapy treatment performed at the same time as an MRI examination. In the end we compute the spatial distribution of the modification of the relaxation rate in a solution of gold-magnetite NSs under laser illumination. First, the optical cross-sections of a single NP must be extracted (Section II A). Second, these properties are used to spatially map the temperature increase collectively generated by the multitude of NPs in the solution (Section II B). Third, the generated map serves as a basis to apply the analytical theory of relaxation induced by superparamagnetic NPs in order to obtain the corresponding map of the relaxation rate modification (Section II C).

The laser irradiance is set to 1.15 W/cm^2, which is close to the maximum permissible irradiance exposure for human skin at 1000 nm[23] and its beam radius is 0.28 cm, in agreement with an experimental setup from the literature[24]. The baseline temperature of the sample is set to 310 K to align with the temperature of the human body. An ideal case without aggregation is considered here.

A. Optical cross-sections of the gold-magnetite NSs

The first step is to determine the absorption and scattering cross-sections of a single NS. We employ the finite element method software COMSOL Multiphysics to solve Maxwell's equations and extract the cross-sections. These simulations were conducted in 3D using the Electromagnetic Waves, Frequency Domain interface. Data for the dielectric function of gold were obtained from [25], and those for magnetite from [26]. Because the mean free path of free electrons is comparable to or larger than the dimensions of the gold shell, we

apply a correction to the gold dielectric function [27]. We aim at highlighting the maximum potential of each NS geometry for use as a photothermal agent, so the position of the peak absorption maximum will be reported later on. We limit our analysis to peaks within the near-infrared human biological window, ranging from 650 nm to 1350 nm. This range corresponds to wavelengths where light achieves its maximum penetration depth in tissue[28].

As we discuss about the use of NSs in MRI, it is important to consider the potential effect of an external magnetic field on their plasmonic resonances. If we want to simulate a phototherapy treatment performed simultaneously with an MRI examination, we should also discuss the modification of the optical properties of our NPs when they are immersed in a constant magnetic field, which is the bore of MRI. A constant magnetic field has the effect of splitting the plasmonic resonance of metallic NPs when illuminated with linearly polarized light. This phenomenon is due to the difference in absorption between left-circularly polarized light and right-circularly polarized light. However, this split requires a very high magnetic field, and is too small to be observed experimentally at normal field strenghts[29]. At 30 Tesla the absorption peak wavelength shifts by only 1 nanometer for silver NPs[30]. Since the magnetic field used in MRI is generally on the order of a few Tesla[31], the magneto-optical effects are negligible.

B. Temperature elevation due to laser illumination

Although plasmonic NPs are well-known for efficient light energy conversion into heat, due to the low laser powers used in the biomedical field, a single NP alone generates a too low nanoscopic temperature gradient to have any impact on relaxation. Indeed, an irradiance of 10 000 W/cm^2 is necessary to achieve a temperature increase of several degrees in the vicinity of a *single* gold NP submerged in water[32]. However, the maximum permissible irradiance exposure for human skin is low (~ 1 W/cm^2), which leads to negligible single-particle temperature changes ($< 10^{-4}$ degrees). This fact justifies that the usual MRI relaxation models will be used latter on.

On the other hand, the collective thermal effects of all the NPs creates a macroscopic temperature gradient that can reach the temperature required for phototherapy[10]. The macroscopic temperature rise occurs at a different time scale (1 s) than the nanometric temperature gradient around a single NS (10^{-6} s)[33]. Therefore, to map the steady-state temperature increase inside a solution of NPs a continuous collective model is used[10,34]. In this model the heat transfer is assumed to occur solely through conduction. This collective approach implies open thermal boundary conditions, so with a (quasi-)uniform conductivity around the zone heated by the laser beam. Heat transfer by convection can be neglected due to the low Rayleigh number of water[10], and radiation transfer is also sufficiently low. The NSs are assumed not to aggregate and to have a uniform concentration in the sample. The spatial dependence of the temperature is given by:

$$T_{collective}(\vec{r}) = \iiint_{Laser\ beam} \frac{q(\vec{r'})}{4\ \pi\ \kappa_{env}\ |\vec{r'} - \vec{r}|} d\vec{r'} \tag{1}$$

with the heat power density defined as:

$$q(\vec{r'}) = I(\vec{r'})\ (N\ \sigma_{abs} + A_{water}) \tag{2}$$

with N the number of NSs per m^3, $I(\vec{r'})$ the intensity of the laser beam, σ_{abs} the absorption cross-section of the NSs and A_{water} is the water absorption coefficient expressed in m^{-1}. The constant κ_{env} is the thermal conductivity of the surrounding medium (water in our case, $\kappa_{water} = 0.6071$ W m^{-1} K^{-1}). This choice is justified because the addition of metallic NPs only minimally alters the thermal conductivity of water[35]. We suppose a localized illumination, by a top-hat beam, along a cylindrical volume of radius 0.28 cm (so no laser intensity outside this cylinder), representing the laser beam in the solution (red cylinder entering the sample in Fig. 1b). The Beer-Lambert law is added to account for the exponential decrease of the beam power through the solution (along the z-axis). The expression

employed for the heat power density is the following:

$$q(\vec{r'}) = I_0 \, e^{-(\sigma_{ext} \, N + A_{water}) \, z} \, (N \, \sigma_{abs} + A_{water}) \tag{3}$$

with σ_{ext} the extinction cross-section and z the the z-coordinate as defined in Fig. 1b. Note that the model (Eq. 1) does not account for secondary attenuation from the light scattered by the NPs. Such approximation is valid here due to the relatively low NS concentrations considered[36]. The validity of this model for an open physical system has been experimentally proven[34].

Eq. 1 takes into account the temperature increase due the direct heating of both the solvent and the NPs. Discussing the contribution of the solvent, Terentyuk et al.[24] report a temperature rise of 6 degrees for the solvent (physiological solution) under laser irradiance of 4 W/cm^2. We consider a lower laser irradiance of 1.15 W/cm^2 and water as solvent (with data for A_{water} from [37]). In this case, the solvent contributes negligibly to the temperature increase (on the order of tenths of a degree) for wavelengths below 900 nm. Above 900 nm, it contributes to a temperature increase of approximately 2 degrees.

Subsequently, a temperature map is computed: The sample volume is divided into several voxels (volume elements), and the temperature increase is averaged over each of these voxels. A slice passing through the center of the laser beam is then selected. This plane is represented in a 2D image where each pixel corresponds to a property of the corresponding voxel. This procedure aims to align with the way an MRI signal is represented after signal sampling and a Fourier transform, through an image comprising multiple pixels[31]. The voxel size is chosen to be equal to 1 cubic millimeter to be similar to an MRI pixel[31].

C.   Transverse proton relaxation due to magnetic particles

Superparamagnetic (SPM) NPs act as contrast agents in magnetic resonance imaging. Upon accumulation in specific tissues, they influence the proton relaxation process, thereby altering the longitudinal relaxation rate (R_1) and the transverse relaxation rate (R_2)[38]. The larger these rates, the more efficient the MRI contrast. Different relaxation measurement sequences exist in MRI. In the following we will consider a standard measurement sequence called Carr-Purcell-Meiboom-Gill (CPMG). The latter allows overcoming instrumental magnetic field inhomogeneities by using a succession of excitation and refocusing pulses.

For SPM NPs the relaxation arises from the magnetic inhomogeneities generated by the dipolar magnetic field of the particles. In an aqueous sample each proton undergoes magnetic fluctuations due to its free bulk diffusion in these magnetic inhomogeneities (referred to as the outersphere mechanism). Three different regimes exist for the relaxation induced by SPM NPs at high magnetic field: The Motional Averaging Regime (MAR), the Static Dephasing Regime (SDR), and the Partial Refocusing Model (PRM)[38].

The parameters that determine the relaxation regime of the NP are its radius and magnetization, with the latter defined as the ratio between the amplitude of the magnetic moment and the volume of the NP. The Redfield factor $F_{Redfield}$, defined as the product of the proton Larmor frequency shift at the equator of the particle and the diffusion correlation time[39], allows to determine the relevant regime:

$$F_{Redfield} = \frac{\gamma_p \, \mu_0 \, M_\nu \, R_{NMR}^2}{3 \, D} \tag{4}$$

with $\gamma_p = 2.675 \times 10^8 \, \text{rad} \, \text{s}^{-1} \text{T}^{-1}$ the gyromagnetic ratio of the proton, μ_0 the vacuum permeability equal to $4\pi \times 10^{-7} \text{H} \, \text{m}^{-1}$, M_ν the saturation magnetization of magnetic particles expressed in A m^{-1}, R_{NMR} the minimal NP-proton distance of approach expressed in m, and D the diffusion coefficient of water expressed in m^{2}s^{-1}. In this study, the diffusion coefficient is determined for each pixel based on the mean voxel temperature using data from Easteal et al.[40].
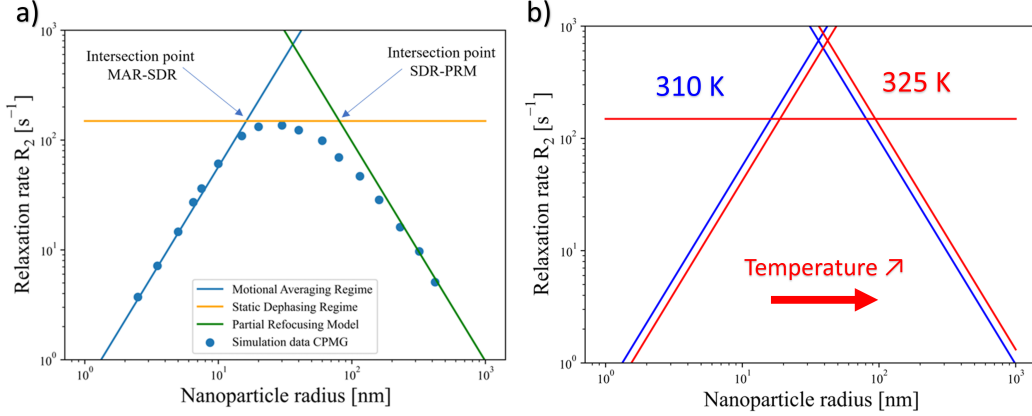
FIG. 2.   a) Models of transverse relaxation caused by magnetic particles at high field (MAR: Blue line, SDR: Orange line, PRM: Green line). The simulation data (blue dots) is sourced from reference[45]. b) Effect of temperature elevation on transverse relaxation. Blue lines: 310 K; red lines: 325 K.

NPs with a $F_{Redfield}$ value below 1 fall into the MAR regime[39]. The equation providing the transverse relaxation in the MAR regime at high magnetic field is:

$$R_2 = \frac{64\pi}{135} \left(\frac{\mu_0}{4\pi}\right)^2 \mu_{SPM}^2 \gamma_p^2 \frac{C}{R_{NMR}D} \tag{5}$$

with μ_{SPM} the SPM NP's magnetic moment and C the NP concentration expressed in m^{-3}. When the size or the magnetization of the NP increases, the protons appear static during the relaxation compared to the NPs. In this regime the SDR model takes over with the following expression for the relaxation rate[41]:

$$R_2 = \frac{2\pi\mu_0}{9\sqrt{3}} C\gamma_p \mu_{SPM} \tag{6}$$

As the size of the NP continues to increase, it reaches a point where the echo time (τ_{echo}) of the CPMG sequence influences relaxation[42]. The PMR predicts:

$$R_2^{CPMG} = 3\pi x^{1/3} CDR_{NMR} \left[1.34 + \frac{4\pi CR_{NMR}^3}{3}x\right]^{5/3} \tag{7}$$

$$x = \sqrt{\frac{1}{20}} \gamma_p \mu_0 \frac{\mu_{SPM}}{\pi R_{NMR}^3} \tau_{echo} \tag{8}$$

The three different relaxation models used in this study are summarized in Fig. 2a. The three straight lines representing the various models take the form of a hat, on such a log-log graphical representation. This is related with an optimal NP size that maximizes the R_2 relaxation rate[43], as indicated by the more detailed simulation results (blue dots in Fig. 2a). Note that the simulation results (blue dots) agree well with the models (lines), especially for smaller radii, which is the most interesting regime later on. Magnetic resonance thermometry has been experimentally verified using these relaxation models[44].

Upon heating, the sample temperature impacts the relaxation rate R_2 by altering the water diffusion coefficient D, higher temperature leading to larger D. Thus, an increase in temperature will shift the lines associated with the models to the right (blue hat to red hat in Fig. 2b), indeed D is in the denominator of Eq. 5 (MAR model), but in the numerator of Eq. 7 (PRM model).

Contrarily to classical pure magnetite particles, the NSs considered here have a gold shell that is impermeable to water molecules; therefore, the R_{NMR} considered for the NPs in the

above models is the total radius of the NS (r_{core} + t_{shell}). In relaxation models, NSs can be treated by considering the dilution of the magnetic moment μ_{SPM} of the magnetite core within the total volume occupied by the NS[38].

In the research field dedicated to superparamagnetic contrast agents, it is common to fix the iron concentration to compare different contrast agents. Therefore, we are working with a fixed iron concentration in this study (0.2 mM), as mentionned in Section I.

In each voxel of the temperature map obtained in the previous step, a discrimination procedure is applied to determine which relaxation model must be used, via the calculation of $F_{Redfield}$. We compare this value to the pivot value of $F_{Redfield}$ calculated from the intersection of the MAR (Eq. 5) and SDR (Eq. 6) models. This first step determines whether the MAR model should be used. To discriminate between the SDR and PRM, both relaxation values are calculated and compared (Eqs. 6-7), and the model returning the smaller value is then chosen. This workaround allows us to bypass the issue of calculating the intersection between the SDR and PRM models. The intersection between the MAR model and the SDR model, on the other hand, can be found analytically.

To quantify the illumination impact on R_2, we define its change:

$$\Delta R_2 = \left(\frac{R_{2\ focus} - R_{2\ amb}}{R_{2\ amb}} \right) \times 100 \tag{9}$$

where $R_{2\,focus}$ is the extremum value for R_2, so which is most changed with respect to the ambient value $R_{2\,amb}$ (uniform 310 K human body temperature, no illumination). This extremum value $R_{2\,focus}$ is a maximum or a minimum that appears at the warmest point of the temperature profile. Note that both $R_{2\,amb}$ and $R_{2\,focus}$ depend on the specific NS geometry employed, where $R_{2\,amb}$ is calculated via the constant 310 K, and $R_{2\,focus}$ is determined via the detailed temperature map focal point.

III. RESULTS

The following section is divided into three parts: The first reports the results obtained for the optical properties of NPs, the second deals with the temperature elevation by laser illumination, and the final part discusses the influence of temperature increase on the transverse relaxation rate R_2. This last part shows a significant influence of the temperature on the R_2 in the case of small particles.

A. Obtained optical cross-sections of the gold-magnetite NSs

The evolution of the absorption spectrum with the core radius for a gold-magnetite NS, with a fixed thickness gold shell (10 nm), is depicted in Fig. 3a (COMSOL simulations, see Section II A). The human near-infrared biological window is highlighted in orange, ranging from 650 nm to 1350 nm. For smaller radii, a single peak is observed in the absorption spectrum, whereas for larger radii, three peaks are present. The emergence of these peaks is attributed to the interaction between the sphere and cavity plasmons[46]. As the NP size increases, more modes can be excited.

The different modes between the inner and the outer metallic surfaces of the sphere and the cavity will couple together, giving rise to a complex spectrum. Using Mie theory for multi-layered shells or multipole decomposition[47,48], the nature and relative contribution of the modes (such as dipolar or quadrupolar) can be calculated (not shown), or one can inspect the global field profiles. The peak appearing around 500 nm (for $r_{core} > 40$ nm, left side of Fig. 3a) is attributed to the magnetic dipole mode. The central peak corresponds to the electric quadrupole mode (see red dash-dotted guide-line) and the rightmost peak in the spectrum is the electric dipole mode (see blue dash-dotted guide-line). The respective mode profiles are shown in Fig. 3b).
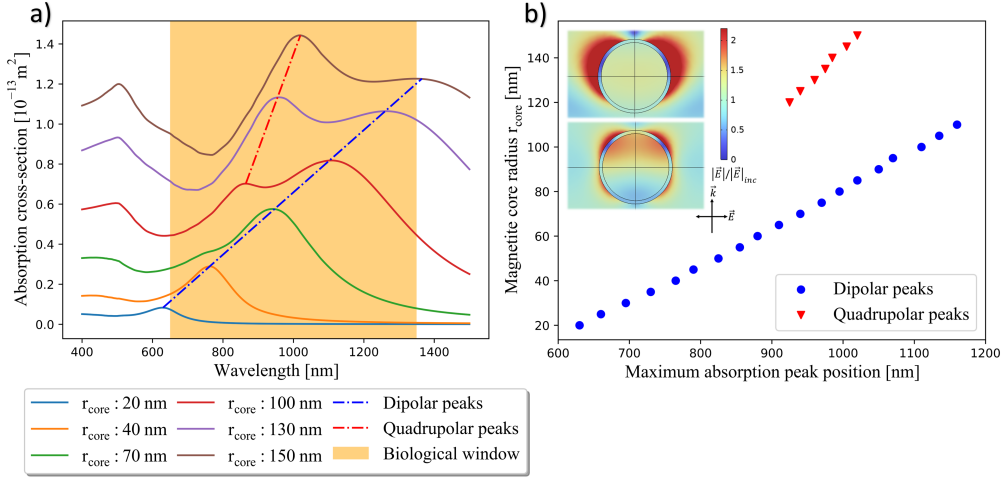
FIG. 3.   a) Absorption spectrum for NSs with a 10 nm gold shell and a variable r_{core}. Increasing the core radius leads to the appearance of a new absorption peak in the biological window. b) Position of the largest absorption peak in the biological window as a function of r_{core} for a fixed shell thickness of 10 nm. **Inset**: Profile of the electric field around the NP for $r_{core} = 100$ nm (upper inset: Dipolar mode, lower inset: Quadrupolar mode). In the case of $r_{core} = 100$ nm, the electric dipolar mode exhibits higher absorption than the quadrupolar mode, so we would excite at the wavelength (1115 nm) with the maximum of the electric dipolar mode.

As the size of the magnetite core increases, the electric dipole peak shifts rapidly to the right. When the electric dipole peak exits the biological window, the quadrupole peak becomes the most important one, from a radius of about 130 nm. This allows NPs with a larger magnetite core to still possess an absorption peak within the biological window. We can also observe that absorption increases with the core radius (curves shift upwards in Fig. 3a). This is an expected phenomenon since increasing the core radius requires more gold to form the shell, and it is understood that absorption scales with plasmonic metal volume[49].

Fig. 3b depicts the evolution of the position of the absorption peak maximum for a NP with a variable core radius and a fixed shell thickness of 10 nm. Here, we consider only the peaks located within the human biological window, so the dipole and quadrupole mode, with their corresponding core radius r_{core}. For the fixed shell thickness of 10 nm, the r_{core} must be above about 20 nm to yield a usable peak. We limit r_{core} to a maximum of 150 nm to remain within the range of synthesizable magnetite NPs[50].

The results regarding the optimization of t_{shell} are depicted in Fig. 4, with Fig. 4a for $t_{shell} = 50$ nm, and Fig. 4b for $t_{shell} = 150$ nm. This data (also checked for other radii, not shown) reveals that the optimal shell thickness to achieve maximum absorption in the biological window is around 10 nm, see the large overlap between the orange curves in Figs. 4a and b and the biological window. This holds true regardless of which mode dominates within the biological window, be it the dipolar (Fig. 4a for smaller r_{core}) or quadrupolar (Fig. 4b for larger r_{core}) mode. Thus, in order to maximize the heating efficiency of the considered NSs, we chose the shell thickness $t_{shell} = 10$ nm for the remainder of this work. It should be noted for $t_{shell} = 5$ nm in Fig. 4b that the dipolar resonance peak is outside the frequency range considered here, which gives it a particular shape.

B.   Mapping of the temperature elevation due to laser illumination

The temperature maps were calculated for different sizes of magnetite cores r_{core} and a fixed gold shell thickness of 10 nm (see Fig. 5), the iron concentration is set at 0.2 mM.
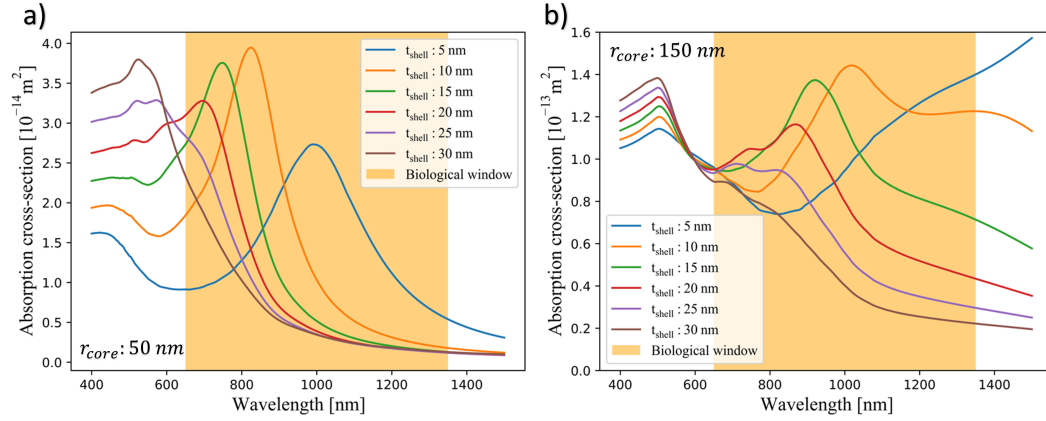
FIG. 4.   Optimization of the NP shell thickness. a) Absorption spectrum for NSs with a 50 nm r_{core} and a variable gold shell: In this case, it is the dipolar peak that is exclusively present in the biological window. b) Absorption spectrum for NSs with a 150 nm r_{core} and a variable gold shell: The quadrupolar peak dominates the dipolar peak in the biological window.

Each NP solution is illuminated at its maximum absorption peak (see Fig. 3b, each r_{core} corresponds to a specific excitation wavelength). The temperature maps are generated using the collective thermal model (Eq. 1) utilizing data from optical simulations (absorption cross-sections σ_{abs} at the excitation wavelength, see Section III A).
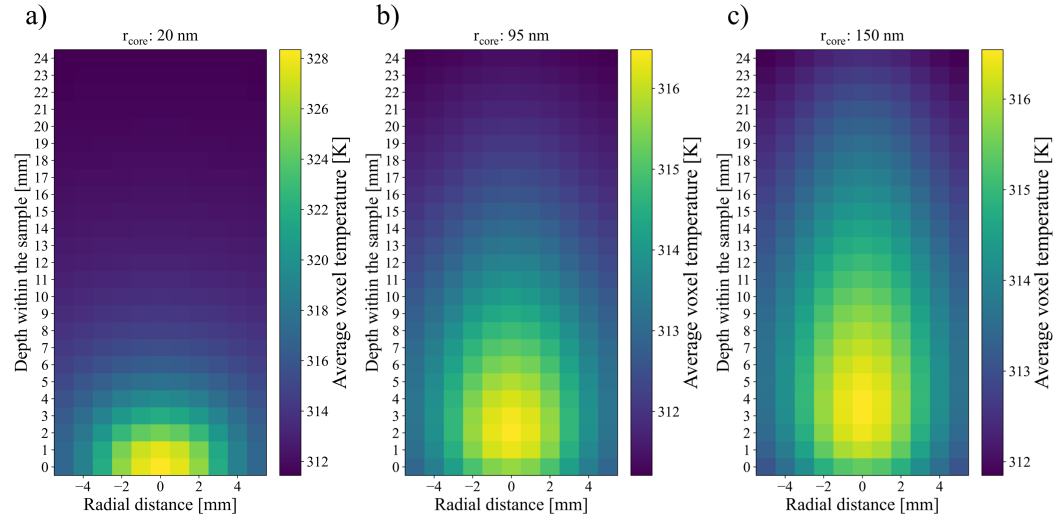

FIG. 5.   Map of the temperature after laser illumination. a) r_{core}: 20 nm. Gold concentration: 0.69 mM. NS concentration: 8.875×10^{16} m^{-3}. b) r_{core}: 95 nm. Gold concentration: 0.10 mM. NS concentration: 8.28×10^{14} m^{-3}. c) r_{core}: 150 nm. Gold concentration: 0.062 mM. NS concentration: 2.10×10^{14} m^{-3}.

For a small core radius of magnetite of 20 nm (Fig. 5a), the temperature increase obtained after illumination is significant, around 18 degrees (background temperature fixed at 310 K). However, this heating is localized near the laser impact point, mainly due to the high NS concentration. In contrast, for larger r_{core} of 95 nm (Fig. 5b) and 150 nm (Fig. 5c), the temperature increase is smaller, around 6 degrees, but it is more diffuse throughout the sample. This can be explained by the fact that the NP concentration and the gold concentration in the different samples inevitably vary with the size of the magnetite core

due to the fixed iron concentration. Even though the absorption cross-section increases with the growing size of NPs, the particle concentration decreases significantly. The NP size variation alters the excitation wavelength used, which also leads to a modification of the water absorption coefficient. We can observe that all three NP geometries generate a sufficient temperature increase to fall within the minimum range of 3 to 7 degrees required for phototherapy[9].

C.   Temperature influence on the relaxation time

ΔR_2 as a function of r_{core} (at a fixed iron concentration of 0.2 mM, with a gold shell thickness of 10 nm) is shown on Fig. 6. We can distinguish the three different relaxation regimes (MAR, SDR or PRM) in the figure, indicating which model is appropriate at the extremum point for R_2 (called $R_{2\,focus}$): The MAR regime extends below r_{core} around 25 nm, SDR is from 25 nm to 90 nm, and PRM extends above 90 nm.

For NPs in the MAR regime, a 30% decrease of the relaxation rate is observed, for r_{core} below 20 nm. Between 20 and 25 nm, the transition between the MAR and SDR regime occurs, during which ΔR_2 is highly dependent on r_{core}. In the SDR regime, temperature has no influence on relaxation, so ΔR_2 remains 0. Between 90 and 100 nm, the transition between the SDR and PRM regime occurs. An increase in the relaxation rate of about 20% can be observed in the PRM regime. The jump in ΔR_2 around 120 nm radius is attributed to the transition from the dipolar peak to the quadrupolar peak, so we keep an excitation wavelength in the biological window (see Fig. 3b). The shape of the curve observed between 120 and 150 nm is explained by the variation in the water absorption coefficient between wavelengths of 900 nm and 1050 nm, indicating a strong contribution from the solvent in this range. Although nanoparticles of these sizes show a 20% change in ΔR_2, their efficiency is partially due to the heating of the solvent. For biomedical applications, nanoparticles between 20 and 25 nm are preferred, as they do not require excitation wavelengths that significantly heat the water. This allows for better laser penetration into human tissues, resulting in a more effective therapy.

The inset in Fig. 6 shows the relaxation rate R_2 directly. Circular blue points represent data calculated at background temperature (i.e. without laser illumination), while triangular orange points represent data after laser illumination. As expected, the values obtained for laser illumination are shifted to the right compared to those calculated at background temperature.

The intersections between the models (MAR-SDR and SDR-PRM) in Fig. 6 and Fig. 2 are not identical, which is due to the addition of the gold shell. Indeed, besides increasing the size for each NP, we also increase the total volume in which the magnetization of the magnetite core will be diluted, which results in shifted model intersections.

If we compare the position of the absorption peak in the biological window (Fig. 3b) and the modification of the relaxation rate (Fig. 6), we see that there is a range of r_{core} between 20 and 25 nm that allows a significant modification of the relaxation rate (large $|\Delta_{R_2}|$) and an absorption peak at the beginning of the biological window (around 630-670 nm). Thus, NPs with r_{core} between 20 nm and 25 nm and a t_{shell} of 10 nm could serve as theranostic agents, with their heating monitored by MRI.

Fig. 7 displays three maps of relaxation rates for the three geometries from Fig. 5. For $r_{core} = 20$ nm (Fig. 7a), the relaxation regime is MAR everywhere. This particle size leads to a reference $R_2 = 141\ \mathrm{s}^{-1}$ at the background temperature 310 K (see Fig. 6 inset, blue dots). Therefore, the laser illumination decreases the relaxation rate with about 30% in an area extending up to 5 mm in the sample.

For $r_{core} = 95$ nm (Fig. 7b), interestingly, we have a critical size where both SDR and PRM regimes are present in the map. Below a depth of about 17-21 nm in the sample, we need to use SDR (yellow zone). Beyond this transition depth, we need to apply PRM (blue zone), as the different temperature (Fig. 5b) leads to a different local Redfield parameter $F_{Redfield}$. Indeed, laser illumination increases the water diffusion coefficient, causing a decrease in
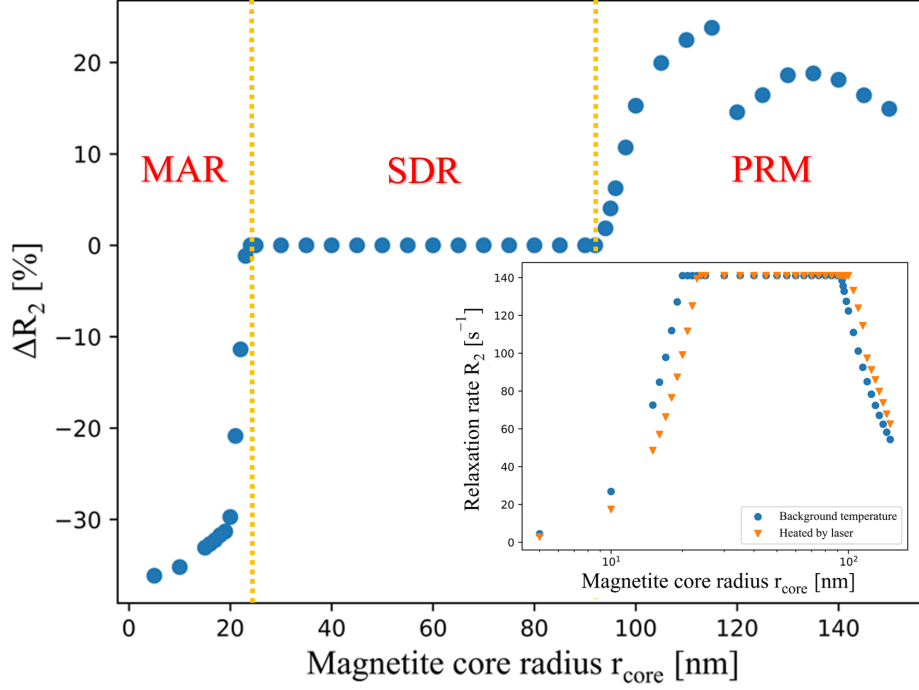
FIG. 6. ΔR_2 as a function of r_{core}. Significant decrease (-30%) in the relaxation rate due to laser illumination between 20 and 25 nm for r_{core}. Significant increase (+20%) for r_{core} above 100 nm. The three relaxation regimes are delimited by dashed orange vertical lines. **Inset**: Relaxation rate R_2 as a function of r_{core}.

the value of the Redfield factor. This allows the NP to shift in the SDR regime in the warm zone. When laser illumination no longer produces enough heat, due to decreasing irradiance with the distance traveled in the sample (Eq. 3), the Redfield coefficient will increase, causing the NSs to return into the PRM regime. Overall there is only a small change of R_2, with respect to the background value $R_2 = 135 \mathrm{\ s}^{-1}$, corresponding to the background temperature of 310 K, in the PRM regime for this size.

For $r_{\mathrm{core}} = 150$ nm (Fig. 7c), the relevant relaxation regime is PRM, with a background $R_2 = 54 \mathrm{\ s}^{-1}$. The laser illumination slightly increases the relaxation rate in an area that extends up to half of the sample, but overall the values are much lower than in Fig. 7a and Fig. 7b. This is because larger particles correspond to a lower NS concentration, due to the fixed iron concentration (downward right side of the hat in the inset of Fig. 6).

In general, we observe qualitatively different trends as a function of the core size. For smaller sizes the warmer zone decreases R_2, whereas for larger sizes the opposite is observed. Furthermore, we see important differences in the penetration distance and modulation effect: Smaller particles have a stronger effect, but over a smaller distance, whereas larger particles lead to a smaller variation of R_2 but over a larger distance. Depending on the particular situation, one should be aware of the different behaviours when combining photothermal therapy and MRI using these hybrid nanoparticles.

IV.   CONCLUSION

This work studies the combination of phototherapy and MRI with an extensive numerical approach. We examine the spatial modification of the transverse relaxation rate R_2 in a uniformly concentrated solution composed of gold-magnetite hybrid NPs under laser
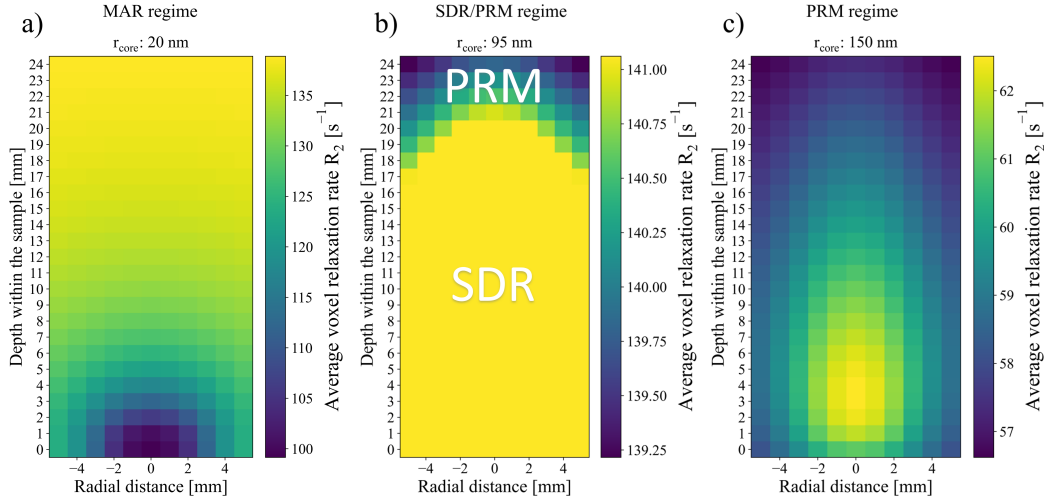
FIG. 7.   Map of the transverse relaxation rate due to laser illumination for a iron concentration of 0.2 mM. The parameters used are as follows: a) r_{core}: 20 nm. Gold concentration: 0.69 mM. Concentration NS: 8.875×10^{16} m^{-3}. b) r_{core}: 95 nm. Gold concentration: 0.10 mM. Concentration NS: 8.28×10^{14} m^{-3}. c) r_{core}: 150 nm. Gold concentration: 0.062 mM. Concentration NS: 2.10×10^{14} m^{-3}.

irradiation. An optimization of this configuration is conducted, revealing that the optimal shell thickness for maximizing absorption within the biological window is 10 nm. Furthermore, it is illustrate that a wide range of r_{core} (20-150 nm) achieves an absorption peak within the human biological window. It is also demonstrated that laser illumination of a solution of NPs, with an iron concentration acceptable for human use, generates sufficient heat for phototherapy. Furthermore, for a certain range of r_{core} for the NPs (5-25 nm and 95-150 nm), the heating alters the relaxation rate of the solution, with the strongest change for small NPs that also have an important and useful optical dipolar resonance peak in the biological window. In addition, depending on the nanoparticle size the position of the maximum R_2 change varies within the sample.

These findings highlight the possibility of real-time monitoring, via MRI, of the temperature increase resulting from phototherapy. For example, this can be used in neuroscience, where NPs under laser illumination are used to directly activate neurons via a temperature increase[51]. Future work can focus on adapting this framework closer to a biological environment, e.g. by taking NP aggregation in cells into account[52] or by including biological tissue turbidity in the modelisation, which could affect the phototherapy and relaxation results.

[1]C. Barca, C. Griessinger, A. Faust, D. Depke, M. Essler, A. Windhorst, N. Devoogdt, K. Brindle, M. Schäfers, B. Zinnhardt, and A. Jacobs, "Expanding Theranostic Radiopharmaceuticals for Tumor Diagnosis and Therapy," Pharmaceuticals **15**, 13 (2021).

[2]F. Chen, E. B. Ehlerding, and W. Cai, "Theranostic Nanoparticles," Journal of Nuclear Medicine **55**, 1919–1922 (2014).

[3]M. V. Efremova, V. A. Naumenko, M. Spasova, A. S. Garanina, M. A. Abakumov, A. D. Blokhina, P. A. Melnikov, A. O. Prelovskaya, M. Heidelmann, Z.-A. Li, Z. Ma, I. V. Shchetinin, Y. I. Golovin, I. I. Kireev, A. G. Savchenko, V. P. Chekhonin, N. L. Klyachko, M. Farle, A. G. Majouga, and U. Wiedwald, "Magnetite-Gold nanohybrids as ideal all-in-one platforms for theranostics," Scientific Reports **8**, 11295 (2018).

[4]D. Maniglio, F. Benetti, L. Minati, J. Jovicich, A. Valentini, G. Speranza, and C. Migliaresi, "Theranostic gold-magnetite hybrid nanoparticles for MRI-guided radiosensitization," Nanotechnology **29**, 315101 (2018).

[5]C. Hoskins, Y. Min, M. Gueorguieva, C. McDougall, A. Volovick, P. Prentice, Z. Wang, A. Melzer, A. Cuschieri, and L. Wang, "Hybrid gold-iron oxide nanoparticles as a multifunctional platform for biomedical application," Journal of Nanobiotechnology **10**, 27 (2012).

[6]M. A. M. Tarkistani, V. Komalla, and V. Kayser, "Recent Advances in the Use of Iron–Gold Hybrid Nanoparticles for Biomedical Applications," Nanomaterials **11**, 1227 (2021).

[7]Y.-D. Xiao, R. Paudel, J. Liu, C. Ma, Z.-S. Zhang, and S.-K. Zhou, "MRI contrast agents: Classification and application (Review)," International Journal of Molecular Medicine **38**, 1319–1326 (2016).

[8]D. Kim and H. Kim, en"Numerical study on optimization of quantitative treatment conditions for skin cancer photothermal therapy considering multiple blood vessels," Computer Methods and Programs in Biomedicine **240**, 107738 (2023).

[9]K. Ahmed, Y. Tabuchi, and T. Kondo, "Hyperthermia: an effective strategy to induce apoptosis in cancer cells," Apoptosis **20**, 1411–1419 (2015).

[10]G. Baffou, *Thermoplasmonics: Heating Metal Nanoparticles Using Light*, 1st ed. (Cambridge University Press, 2017).

[11]M. S. Kang, S. Y. Lee, K. S. Kim, and D.-W. Han, "State of the Art Biocompatible Gold Nanoparticles for Cancer Theragnosis," Pharmaceutics **12**, 701 (2020).

[12]J. Wahsner, E. M. Gale, A. Rodríguez-Rodríguez, and P. Caravan, "Chemistry of MRI Contrast Agents: Current Challenges and New Frontiers," Chemical Reviews **119**, 957–1057 (2019).

[13]L. R. Hirsch, R. J. Stafford, J. A. Bankson, S. R. Sershen, B. Rivera, R. E. Price, J. D. Hazle, N. J. Halas, and J. L. West, "Nanoshell-mediated near-infrared thermal therapy of tumors under magnetic resonance guidance," Proceedings of the National Academy of Sciences **100**, 13549–13554 (2003).

[14]S. V. Salihov, Y. A. Ivanenkov, S. P. Krechetov, M. S. Veselov, N. V. Sviridenkova, A. G. Savchenko, N. L. Klyachko, Y. I. Golovin, N. V. Chufarova, E. K. Beloglazkina, and A. G. Majouga, "Recent advances in the synthesis of Fe3O4@AU core/shell nanoparticles," Journal of Magnetism and Magnetic Materials **394**, 173–178 (2015).

[15]A. Billen, A. De Cattelle, J. K. Jochum, M. J. Van Bael, J. Billen, J. W. Seo, W. Brullot, G. Koeckelberghs, and T. Verbiest, "Novel synthesis of superparamagnetic plasmonic core-shell iron oxide-gold nanoparticles," Physica B: Condensed Matter **560**, 85–90 (2019).

[16]N. Harris, M. J. Ford, and M. B. Cortie, "Optimization of Plasmonic Heating by Gold Nanospheres and Nanoshells," The Journal of Physical Chemistry B **110**, 10701–10707 (2006).

[17]A. Majouga, M. Sokolsky-Papkov, A. Kuznetsov, D. Lebedev, M. Efremova, E. Beloglazkina, P. Rudakovskaya, M. Veselov, N. Zyk, Y. Golovin, N. Klyachko, and A. Kabanov, "Enzyme-functionalized gold-coated magnetite nanoparticles as novel hybrid nanomaterials: Synthesis, purification and control of enzyme function by low-frequency magnetic field," Colloids and Surfaces B: Biointerfaces **125**, 104–109 (2015).

[18]T. Jafari, A. Simchi, and N. Khakpash, "Synthesis and cytotoxicity assessment of superparamagnetic iron–gold core–shell nanoparticles coated with polyglycerol," Journal of Colloid and Interface Science **345**, 64–71 (2010).

[19]J. A. Tate, A. A. Petryk, A. J. Giustini, and P. J. Hoopes, "In vivo biodistribution of iron oxide nanoparticles: an overview," (San Francisco, California, USA, 2011) p. 790117.

[20]W. Brullot, V. K. Valev, and T. Verbiest, "Magnetic-plasmonic nanoparticles for the life sciences: calculated optical properties of hybrid structures," Nanomedicine: Nanotechnology, Biology and Medicine **8**, 559–568 (2012).

[21]C. Caro, F. Gámez, P. Quaresma, J. M. Páez-Muñoz, A. Domínguez, J. R. Pearson, M. Pernía Leal, A. M. Beltrán, Y. Fernandez-Afonso, J. M. De La Fuente, R. Franco, E. Pereira, and M. L. García-Martín, "Fe3O4-Au Core-Shell Nanoparticles as a Multimodal Platform for In Vivo Imaging and Focused Photothermal Therapy," Pharmaceutics **13**, 416 (2021).

[22]S.-K. Cheong, S. Krishnan, and S. H. Cho, "Modeling of plasmonic heating from individual gold nanoshells for near-infrared laser-induced thermal therapy," Medical Physics **36**, 4664–4671 (2009).

[23]X. Wu, Y. Suo, H. Shi, R. Liu, F. Wu, T. Wang, L. Ma, H. Liu, and Z. Cheng, "Deep-Tissue Photothermal Therapy Using Laser Illumination at NIR-IIa Window," Nano-Micro Letters **12**, 38 (2020).

[24]G. S. Terentyuk, G. N. Maslyakova, L. V. Suleymanova, N. G. Khlebtsov, B. N. Khlebtsov, G. G. Akchurin, I. L. Maksimova, and V. V. Tuchin, "Laser-induced tissue hyperthermia mediated by gold nanoparticles: toward cancer phototherapy," Journal of Biomedical Optics **14**, 021016 (2009).

[25]P. B. Johnson and R. W. Christy, "Optical Constants of the Noble Metals," Physical Review B **6**, 4370–4379 (1972).

[26]V. Goossens, J. Wielant, S. Van Gils, R. Finsy, and H. Terryn, "Optical properties of thin iron oxide films on steel," Surface and Interface Analysis **38**, 489–493 (2006).

[27]O. Peña, U. Pal, L. Rodríguez-Fernández, and A. Crespo-Sosa, "Linear optical response of metallic nanoshells in different dielectric media," Journal of the Optical Society of America B **25**, 1371 (2008).

[28]S. Asadi, L. Bianchi, M. De Landro, S. Korganbayev, E. Schena, and P. Saccomandi, "Laser-induced optothermal response of gold nanoparticles: From a physical viewpoint to cancer treatment application," Journal of Biophotonics **14** (2021).

[29]G. Armelles, A. Cebollada, A. García-Martín, and M. U. González, "Magnetoplasmonics: Combining

Magnetic and Plasmonic Functionalities," Advanced Optical Materials **1**, 10–35 (2013).

[30] A. Gabbani, G. Campo, V. Bonanni, P. Van Rhee, G. Bottaro, C. De Julián Fernández, V. Bello, E. Fantechi, F. Biccari, M. Gurioli, L. Armelao, C. Sangregorio, G. Mattei, P. Christianen, and F. Pineider, "High Magnetic Field Magneto-optics on Plasmonic Silica-Embedded Silver Nanoparticles," The Journal of Physical Chemistry C **126**, 1939–1945 (2022).

[31] J. T. Bushberg, ed., *The essential physics of medical imaging*, 3rd ed. (Wolters Kluwer Health/Lippincott Williams & Wilkins, Philadelphia, 2012).

[32] A. O. Govorov, W. Zhang, T. Skeini, H. Richardson, J. Lee, and N. A. Kotov, "Gold nanoparticle ensembles as heaters and actuators: melting and collective plasmon resonances," Nanoscale Research Letters **1**, 84 (2006).

[33] P. Keblinski, D. G. Cahill, A. Bodapati, C. R. Sullivan, and T. A. Taton, "Limits of localized heating by electromagnetically excited nanoparticles," Journal of Applied Physics **100**, 054305 (2006).

[34] H. H. Richardson, M. T. Carlson, P. J. Tandler, P. Hernandez, and A. O. Govorov, "Experimental and Theoretical Studies of Light-to-Heat Conversion and Collective Heating Effects in Metal Nanoparticle Solutions," Nano Letters **9**, 1139–1146 (2009).

[35] N. Shalkevich, W. Escher, T. Bürgi, B. Michel, L. Si-Ahmed, and D. Poulikakos, "On the Thermal Conductivity of Gold Nanoparticle Colloids," Langmuir **26**, 663–670 (2010).

[36] N. J. Hogan, A. S. Urban, C. Ayala-Orozco, A. Pimpinelli, P. Nordlander, and N. J. Halas, "Nanoparticles Heat through Light Localization," Nano Letters **14**, 4640–4645 (2014).

[37] G. M. Hale and M. R. Querry, en"Optical Constants of Water in the 200-nm to 200-Mm Wavelength Region," .

[38] Q. L. Vuong, P. Gillis, A. Roch, and Y. Gossuin, "Magnetic resonance relaxation induced by superparamagnetic particles used as contrast agents in magnetic resonance imaging: a theoretical review," WIREs Nanomedicine and Nanobiotechnology **9**, e1468 (2017).

[39] Y. Gossuin, E. Martin, Q. L. Vuong, J. Delroisse, S. Laurent, D. Stanicki, and C. Rousseau, "Characterization of commercial iron oxide clusters with high transverse relaxivity," Journal of Magnetic Resonance Open **10-11**, 100054 (2022).

[40] A. J. Easteal, W. E. Price, and L. A. Woolf, "Diaphragm cell for high-temperature diffusion measurements. Tracer Diffusion coefficients for water to 363 K," Journal of the Chemical Society, Faraday Transactions 1: Physical Chemistry in Condensed Phases **85**, 1091 (1989).

[41] R. J. S. Brown, "Distribution of Fields from Randomly Placed Dipoles: Free-Precession Signal Decay as Result of Magnetic Grains," Physical Review **121**, 1379–1382 (1961).

[42] P. Gillis, F. Moiny, and R. A. Brooks, "OnT2-shortening by strongly magnetized spheres: A partial refocusing model," Magnetic Resonance in Medicine **47**, 257–263 (2002).

[43] Q. L. Vuong, J. Berret, J. Fresnais, Y. Gossuin, and O. Sandre, "A Universal Scaling Law to Predict the Efficiency of Magnetic Nanoparticles as MRI T2-Contrast Agents," Advanced Healthcare Materials **1**, 502–512 (2012).

[44] D. Chalise and D. G. Cahill, en"Highly Sensitive and High-Throughput Magnetic Resonance Thermometry of Fluids Using Superparamagnetic Nanoparticles," Physical Review Applied **19**, 014055 (2023).

[45] Q. L. Vuong, P. Gillis, and Y. Gossuin, "Monte Carlo simulation and theory of proton NMR transverse relaxation induced by aggregation of magnetic particles used as MRI contrast agents," Journal of Magnetic Resonance **212**, 139–148 (2011).

[46] E. Prodan, C. Radloff, N. J. Halas, and P. Nordlander, "A Hybridization Model for the Plasmon Response of Complex Nanostructures," Science **302**, 419–422 (2003).

[47] K. Ladutenko, U. Pal, A. Rivera, and O. Peña-Rodríguez, "Mie calculation of electromagnetic near-field for a multilayered sphere," Computer Physics Communications **214**, 225–230 (2017).

[48] R. Alaee, C. Rockstuhl, and I. Fernandez-Corbaton, "An electromagnetic multipole expansion beyond the long-wavelength approximation," Optics Communications **407**, 17–21 (2018).

[49] O. D. Miller, A. G. Polimeridis, M. T. Homer Reid, C. W. Hsu, B. G. DeLacy, J. D. Joannopoulos, M. Soljačić, and S. G. Johnson, "Fundamental limits to optical response in absorptive systems," Optics Express **24**, 3329 (2016).

[50] Q. Li, C. W. Kartikowati, S. Horie, T. Ogi, T. Iwaki, and K. Okuyama, "Correlation between particle size/domain structure and magnetic properties of highly crystalline Fe3O4 nanoparticles," Scientific Reports **7**, 9894 (2017).

[51] A. Garcia-Etxarri and R. Yuste, "Time for NanoNeuro," Nature Methods **18**, 1287–1293 (2021).

[52] E. Karvelas, N. Lampropoulos, L. Benos, T. Karakasidis, and I. Sarris, "On the magnetic aggregation of Fe3O4 nanoparticles," Computer Methods and Programs in Biomedicine **198**, 105778 (2021).